minerals

MDPI

Article

Raman Spectroscopy Studies of Equilibrated Ordinary Chondrites with H and L Group and Shock Metamorphism Degrees

Yikai Zhang [1], Zhipeng Xia [1,2,*], Bingkui Miao [1,2,*], Jing Huang [3], Chuantong Zhang [1,2], Yan Chen [4] and Guozhu Chen [1,2]

1   Institution of Meteorites and Planetary Materials Research, Key Laboratory of Planetary Geological Evolution at Universities of Guangxi Province, Guilin University of Technology, Guilin 541004, China
2   Guangxi Key Laboratory of Hidden Metallic Ore Deposits Exploration, Guilin University of Technology, Guilin 541000, China
3   Polar Research Institute of China, Shanghai 200136, China
4   International Center for Planetary Science, College of Geosciences, Chengdu University of Technology, Chengdu 610059, China
*   Correspondence: xiazhipeng@glut.edu.cn (Z.X.); miaobk@glut.edu.cn (B.M.)

Abstract: Ordinary chondrites are the most common type of chondrites. As a non-destructive, rapid, and semi-quantitative technology, Raman spectroscopy is widely used in geoscience. This paper presents the results of a Raman spectroscopic study that we conducted for 16 ordinary chondrites with different chemical groups and variable degrees of shock metamorphism. We found that: (1) the relationship between the Fe composition of olivine and pyroxene and the characteristic peaks of the Raman spectrum established by predecessors cannot be refined to the range of meteorites, the shock on meteorites also affects the Raman spectral characteristics of minerals and (2) the full width at half maximum (FWHM) of the shocked minerals (including high-pressure minerals) in meteorites increases in the Raman spectrum, however, no clear numerical relationship with pressure was found. Based on these data, we assess that the feasibility of Raman spectroscopy for the classification of chemical group and shock metamorphism in ordinary chondrites is not well established.

1. Introduction

Ordinary chondrites account for 80%–90% of the total number of discovered meteorites and represent the most commonly found type of meteorites on earth [1]. The China Antarctic scientific expedition team has collected more than 12,000 meteorites in Antarctica since 1998, but less than half of the samples have been classified, so far [2,3].

The chemical groups of ordinary chondrites were subdivided into three types which have different amounts of metal and different amounts of total iron: H, L, and LL [1,4]. The current classification standard of chemical groups was introduced after a refinement of the classification by Grossman and Rubin that is based on the chemical composition of fayalite (Fa) and ferrosilite (Fs)—H($Fa_{16.9-20.4}$ and $Fs_{15.7-18.1}$), L($Fa_{22.7-25.6}$ and $Fs_{18.7-22.6}$), LL($Fa_{27.0-33.0}$ and $Fs_{23.2-25.8}$) [5]. The chemical classification scheme is highly accurate, but the sample preparation process and the analysis are complex and time consuming, and the samples are partially destroyed [6,7]. In addition, physical properties, including density and magnetic susceptibility, are used to classify ordinary chondrites [8]. The main disadvantage of physical classification is the low accuracy. Due to the uneven distribution of chondrites in minerals, the local physical characteristics, such as the magnetic susceptibility and density, do not represent the type of meteorites concisely. Therefore, the classification of large quantities of meteorite samples cannot be appropriately conducted in a fast and yet precise way using the currently available conventional methods.

Shock metamorphic minerals are common in ordinary chondrites. Most of the minerals of the matrix or fragments of the host rock that occur in shock melting veins underwent phase transformations due to high temperatures and high pressures. The main high-pressure minerals include pyroxene which, crystallized, forms the matrix, melted together with majorite and ferropericlase, and solid phase transition high-pressure minerals, including olivine, pyroxene, and feldspar, which form in the host rock fragments. Evidence for the shock metamorphism that caused the formation of the high-temperature and high-pressure minerals is widely present in meteorites and provides an estimation of the physical conditions during the shock of the parent meteorites [9,10]. Stöffler and Fritz et al. systematically summarized the characteristics and degrees of shock deformation, phase transformation of olivine, pyroxene, and feldspar, and melt development of ordinary chondrites. They subdivided ordinary chondrites into the seven shock stages, S1–S6, and shock melting. The corresponding temperature and pressure conditions were predicted by Stöffler in 1991 and Fritz in 2017 [11–13].

Raman spectroscopy provides information about the structure and composition of minerals and has been increasingly applied in geosciences in recent years. The studies also included in-situ analysis of Martian and lunar rocks [14–16] and the identification of special mineral phases in meteorites [17–19]. In previous studies, the Raman spectrum has been used to determine the correlation between the peak position and the element content of characteristic peaks in the olivine and pyroxene spectra as an alternative method to determine the composition of olivine and pyroxene in ordinary chondrites. The data were used to evaluate their classification into the chemical groups of ordinary chondrites [20–23]. However, due to the limited amount of experimental data, the classification standards of chemical groups that were established in previous studies remained controversial.

Crystal chemistry studies show that at room temperature and normal pressure, the larger the M2 unit (including Mn and Ca) and the more twisted the M1 unit (including Fe, Ni, Zn), the more that divalent cations will take priority [24]. The silicon-oxygen tetrahedra in olivine are isolated and not directly connected. Divalent cations connect the silicon oxygen tetrahedrons (Mg^{2+} and Fe^{2+}) residing in octahedral spaces. The Raman characteristic peak of olivine is caused by the vibration of the Si-O bond in the silicon oxygen tetrahedron, so the change in the Raman characteristic peak reflects the vibration of the Si-O bond in the silicon oxygen tetrahedron of olivine.

We studied 16 samples of ordinary chondrites that were discovered by the China Antarctic scientific expedition team in the Grove Mountain, Antarctica (Figure 1 and Table 1). Combined with mineral compositional data on olivine and pyroxene, laser Raman spectrometry was used to analyze the samples. Based on the results, we correlated the variation of the peak positions of the Raman spectra with the characteristics of the different compositions of the chemical groups to facilitate the rapid classification of the ordinary chondrites from the Chinese Antarctic scientific expedition.

Table 1. Information on the selected meteorite samples (analysis of these sample components was conducted by electronic probes and raw data provided by the Meteoritical Bulletin Database).

Sample Name	Chemical Group	Petrologic Type	Shock Stage	Weathering	Av.Fa/mol%	Av.Fs/mol%
GRV 090360	L	5	S1	W1	24.12 ± 0.90 (n = 10)	20.74 ± 1.19 (n = 11)
GRV 090361	L	5	S3	W1	21.92 ± 0.63 (n = 10)	18.95 ± 0.71 (n = 11)
GRV 090363	L	5	S5	W1	21.5 ± 0.38 (n = 7)	18.46 ± 0.88 (n = 11)
GRV 090376	L	5	S2	W2	24.96 ± 0.73 (n = 24)	21.33 ± 0.81 (n = 7)
GRV 090379	L	5	S3	W2	25.06 ± 1 (n = 9)	21.13 ± 0.89 (n = 12)
GRV 090380	L	5	S2	W2	23.94 ± 0.54 (n = 12)	20.68 ± 0.71 (n = 12)
GRV 090403	H	5	S2	W2	19.47 ± 0.23 (n = 10)	17.57 ± 0.28 (n = 9)
GRV 090421	H	5	S2	W2	18.36 ± 0.6 (n = 15)	16.62 ± 0.6 (n = 11)
GRV 090448	L	5	S2	W1	23.63 ± 0.67 (n = 11)	20.11 ± 0.48 (n = 13)

Table 1. *Cont.*

Sample Name	Chemical Group	Petrologic Type	Shock Stage	Weathering	Av.Fa/mol%	Av.Fs/mol%
GRV 090449	L	5	S3	W2	23.53 ± 0.73 (n = 13)	19.77 ± 0.32 (n = 9)
GRV 090463	L	5	S4	W2	23.37 ± 0.37 (n = 15)	19.98 ± 0.52 (n = 15)
GRV 090511	L	5	S4	W1	24.34 ± 0.45 (n = 10)	21.57 ± 1.29 (n = 12)
GRV 090517	L	6	S4	W2	24.08 ± 0.32 (n = 13)	20.88 ± 0.38 (n = 12)
GRV 090519	L	5	S2	W1	24.83 ± 0.78 (n = 10)	21.47 ± 0.66 (n = 9)
GRV 090520	L	5	S3	W3	23.74 ± 0.29 (n = 14)	20.14 ± 0.15 (n = 12)
GRV 090521	L	4	S4	W2	25.31 ± 2.03 (n = 13)	21.05 ± 1.33 (n = 16)

Av.Fa/mol% = average Fa/mol%, Av.Fs/mol% = average Fs/mol%.
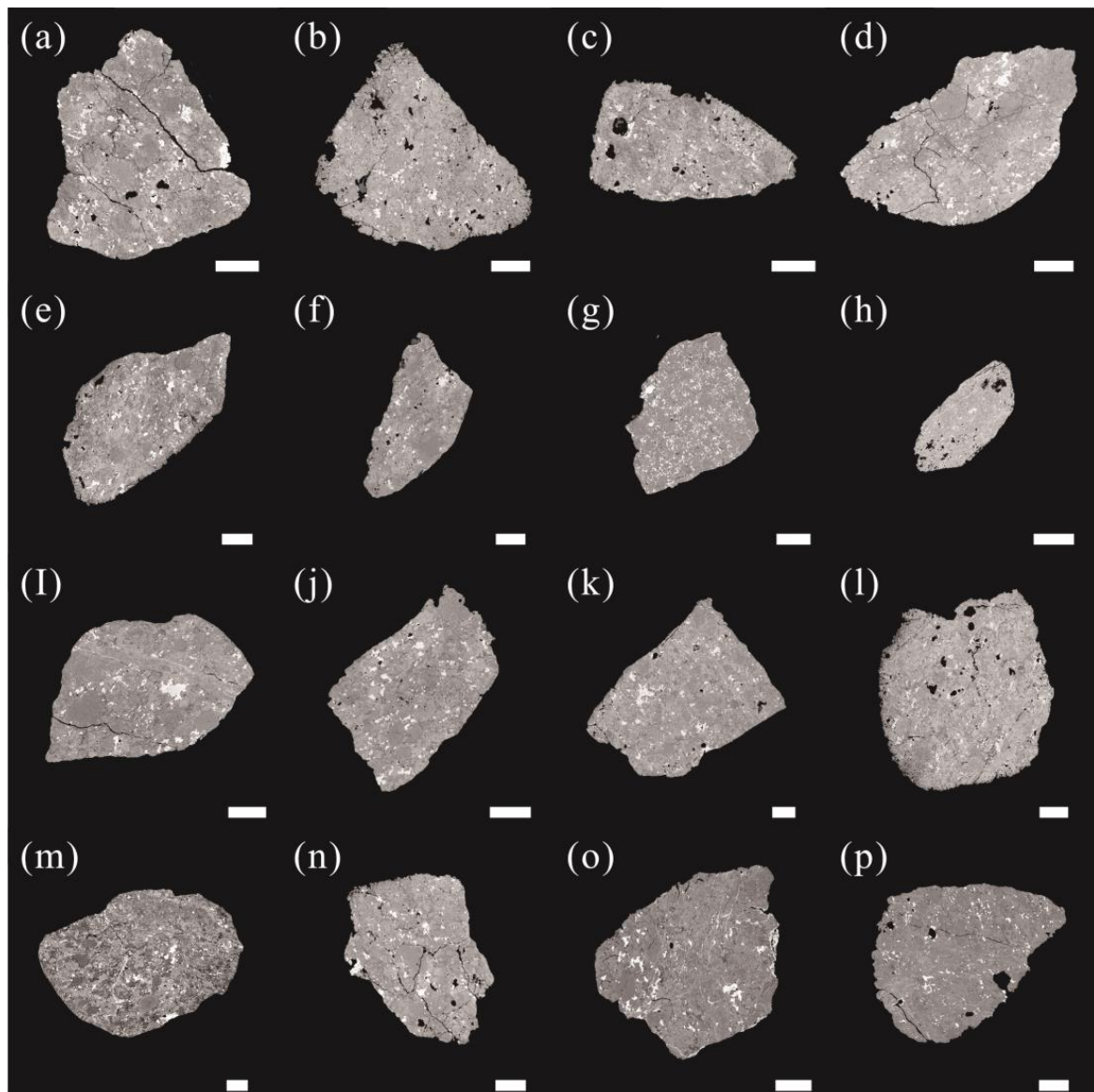
Figure 1. BSE images of 16 samples selected for the study. (**a**) GRV 090360; (**b**) GRV 090361; (**c**) GRV 090363; (**d**) GRV 090376; (**e**) GRV 090379; (**f**) GRV 090380; (**g**) GRV 090403; (**h**) GRV 090421; (**i**) GRV 090448; (**j**) GRV 090449; (**k**) GRV 090463; (**l**) GRV 090511; (**m**) GRV 090517; (**n**) GRV 090519; (**o**) GRV 090520; (**p**) GRV 090521. All pictures are thin section scans. The white bar corresponds to 2 mm.

2. Sample Description and Analytical Methods

In addition to the ordinary chondrite samples, selected olivine and pyroxene Raman data from the RRUFF database were utilized in this study to facilitate the calibration and verification of the experimental results with the specific information given in Table 2.

Table 2. Raman shift of selected minerals (raw data provided by the online database RRUFF).

Minerals	RRUFF ID	Mineral Phase	Peak A/cm^{-1}	Peak B/cm^{-1}	Peak C/cm^{-1}	Fa/mol%	Fs/mol%
	R100103	Fayalite	815.5	838.7		97.7	
	R100104	Fayalite	811.8	840.0		95.2	
	R100102	Fayalite	818.2	845.2		55.5	
	R060539	Forsterite	821.8	853.2		16.5	
	R040057	Forsterite	823.5	855.0		16.1	
	R100101	Forsterite	822.8	854.7		9.19	
Olivine	R050117	Forsterite	823.3	855.0		9.05	
	R060535	Forsterite	823.1	855.0		9.05	
	R040018	Forsterite	822.1	854.0		9.05	
	R060551	Forsterite	823.0	855.1		9.00	
	R100100	Forsterite	823.6	855.8		7.71	
	R100099	Forsterite	824.7	857.0		0.00	
	R040052	Forsterite	822.7	855.2		0.00	
	R040093	Enstatite	337.4	679.8	1007.1		15.2
	R040094	Enstatite	338.2	680.8	1008.9		15.2
	R050644	Enstatite	339.3	682.3	1011.1		10.0
	R060630	Enstatite	350.7	687.7	1014.2		7.30
Pyroxene	R060744	Enstatite	338.7	681.3	1009.3		14.1
	R070418	Enstatite	344.0	683.2	1008.0		14.0
	R070550	Enstatite	340.6	683.3	1011.3		10.0
	R070386	Ferrosilite	330.8	659.0	990.5		82.8
	R070387	Ferrosilite	327.9	669.6	995.8		49.5

We used a Renishaw inVia Raman spectrometer at the Guangxi Key Laboratory of Hidden Metallic Ore Deposits Exploration with a 514 nm Ar+ laser to measure the samples. When the laser reaches the surface of the sample, its power is approximately 10 mW. All analyses were performed under a 100 magnification and 0.85 numerical aperture objective lens with a laser focus of less than 1 μm. The spectral resolution was 1 cm^{-1}, and Raman calibration was performed using monocrystal silicon wafers, with a Raman shift of 520.7 cm^{-1}. From each meteorite 3–5 chondrules were selected for analysis, with 3–5 points per each chondrule, and corrections were made after each test. The Raman spectra were processed with the software OriginPro 2019b.

The composition of olivine and pyroxene in the selected meteorites was determined by electron probe micro analysis (EPMA) at the Institute of Geology and Geophysics and Guangxi Key Laboratory of Hidden Metallic Ore Deposits Exploration using a JOEL JXA-8230 with an acceleration voltage of 15 kV, an acceleration current of 20 nA, and a beam size of 3 μm. The analyses were corrected using the ZAF method [25]. In addition, a Zeiss ΣIGMA field emission scanning electron microscope was used to observe, photograph, and record the microstructure of the samples. The EPMA spots correspond to the Raman test spots with a deviation of less than 1 μm of the position.

3. Results

3.1. Raman Spectrum of Silicate Minerals

The Raman spectral data and EPMA data of all samples are summarized in Tables A1 and A2. The Raman spectrum of sample GRV 090360 is a very typical example for the studied samples (Figure 2). They show two characteristic peaks in the typical Raman spectrum of olivine, termed Peak A, with Raman shift in the range 810–826 cm^{-1} and Peak

B in the range 835–860 cm^{-1}, as well as three characteristic peaks in the typical Raman spectrum of low-Ca pyroxene, termed Peak A, with Raman shift in the range 325–355 cm^{-1}, Peak B in the range 655–690 cm^{-1}, and Peak C in the range 990–1015 cm^{-1}
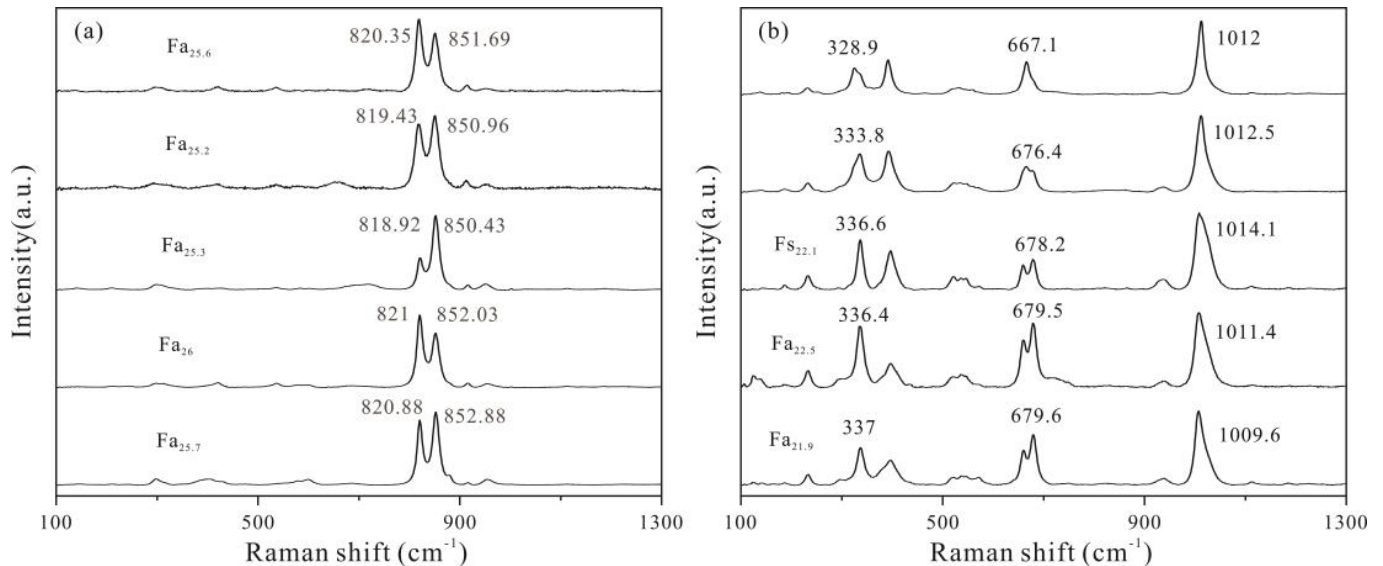
Figure 2. Raman spectra of olivine and pyroxene in GRV 090360. (**a**) is olivine in GRV 090360. (**b**) is pyroxene in GRV 090360.

It should be noted that the Raman spectrum of the low-Ca pyroxene has double peaks at 630–700 cm^{-1}, and Peak B refers to the peak on the right side. Raman spectra with one single peak at 630–700 cm^{-1} would correspond to high-Ca pyroxene. However, high-Ca pyroxene is not considered in the classification of chemical groups in ordinary chondrites, and a discussion of the significance of high-Ca pyroxene is beyond the scope of this paper.

A linear relationship between the Raman characteristic displacement peaks of olivine and the composition of the Mg and Fe endmembers is well known [20]. Therefore, the position changes of the two dominant Raman peaks of olivine in the 800–860 cm^{-1} range can be used as a function of the Fe/(Mg + Fe) ratio to constrain the Fa content of olivine. Samples studied by Pittarello [20] were used in our study as a reference and the following formulae were derived including the data of Pittarello [20]. The results show minor differences from the Pittarello data, with an almost perfect fit (Figure 3a,c):

$$\text{Fa mol\%} = -8.38 X_A + 6902.7 \tag{1}$$

$$\text{Fa mol\%} = -5.36 X_B + 4592.8 \tag{2}$$

The Raman spectrum peaks of low-Ca pyroxene are more complex than those of olivine. Using the available data, we constrained the following formula to constrain the Fe/(Fe + Mg + Ca) ratio of pyroxene (Figure 4a,c,e). The weak fit of equation 3 for pyroxene is mainly related to the influence of two ferropyroxene analyses (R070386 and R070387) in the RRUFF reference data. The determination coefficient (R^2) significantly increases after removing the ferropyroxene data:

$$\text{Fs mol\%} = -2.15 X_A + 746.36 \tag{3}$$

$$\text{Fs mol\%} = -2.76 X_B + 1911.71 \tag{4}$$

$$\text{Fs mol\%} = -2.76X_C + 2798 \tag{5}$$
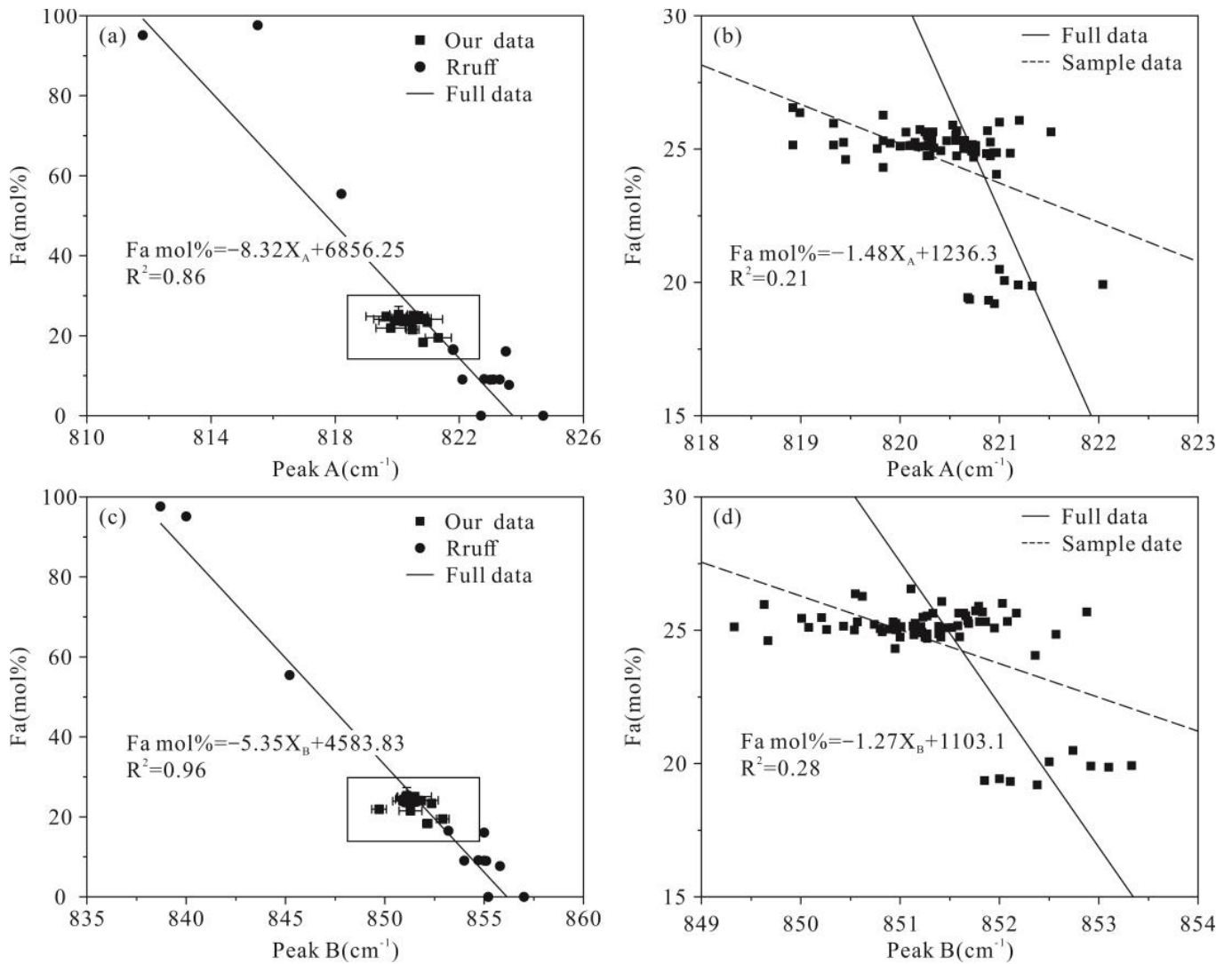
Figure 3. Correlation between the Fa content in olivine and the Raman shift of two selected peaks. (**a,c**) show the results of the fitting from all the data; (**b,d**) show the results of the fitting from our data only. The correlation curve has been calculated using the reference data (circles) and our measurements (filled squares) are plotted for comparison. The error bars represent the standard deviation for 3–5 Raman spectra analyses per chondrite.

However, if we only use our experimental data for fitting, we can see that the determination coefficient of the fitting formula drops significantly; in particular, Peak C of pyroxene is almost irrelevant.
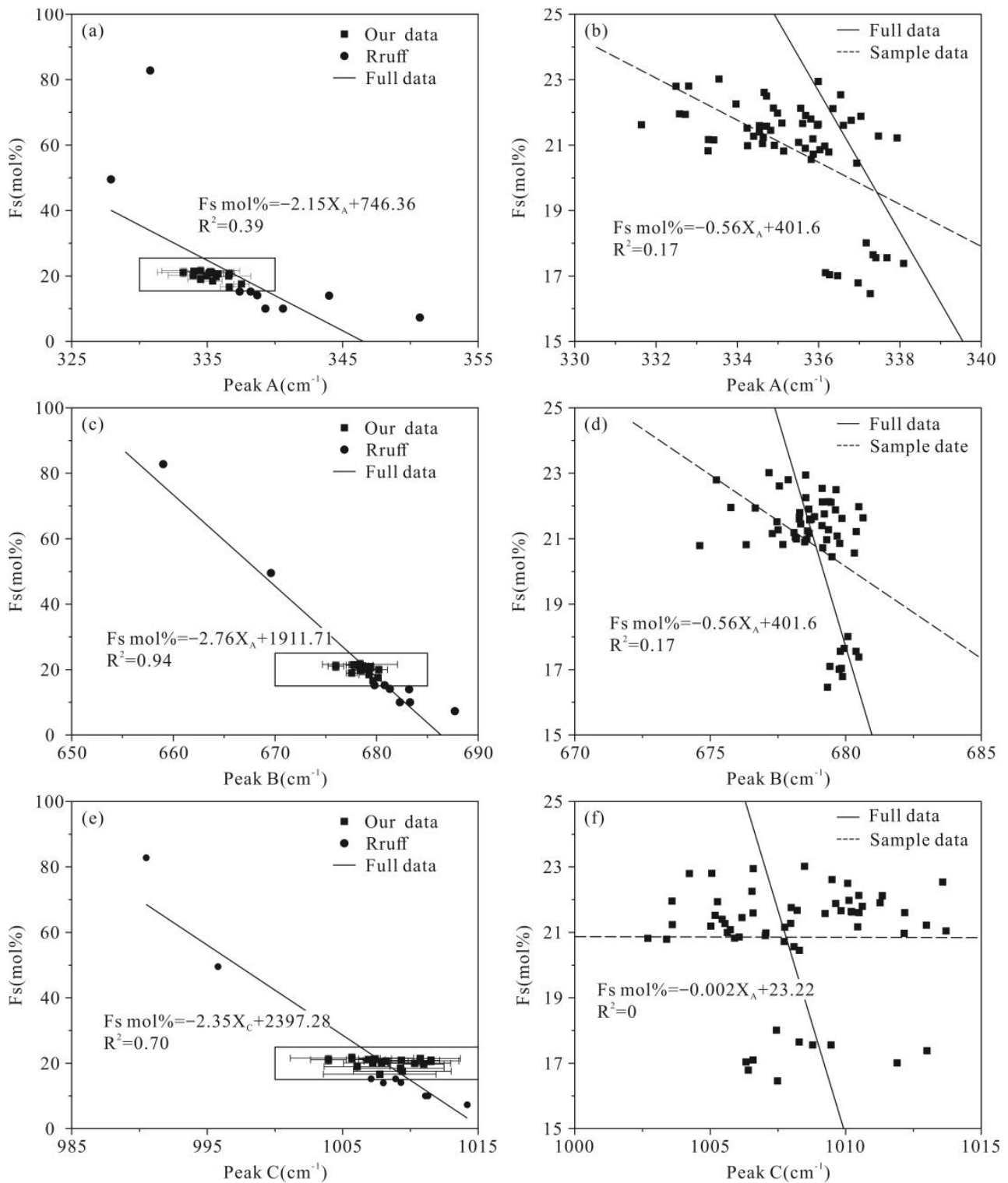
Figure 4. Correlation between the Fs content in olivine and the Raman shift of two selected peaks. (**a,c,e**) show the results of the fitting from all the data. (**b,d,f**) show the results of the fitting from our data only. The correlation curve has been calculated using the reference data (circles) and our measurements (filled squares) are plotted for comparison. The error bars represent the standard deviation for 3–5 Raman spectra analyses per chondrite.

3.2. Raman Spectrum of Shocked Silicate Minerals

Metal-sulfide veins are abundant in H ordinary chondrites. On the surface of two H ordinary chondrite samples, opaque network veins are present (Figure 1g,h). Silicate minerals are strongly fragmented, and the whole sheet shows obvious darkening. BSE images recorded by scanning electron microscopy show that the opaque vein-like domains are composed of a large number of silicate mineral fragments. The minerals are filled with a fine network of metal sulfides, with small amounts of metal sulfides connecting at the edges of the veins. The shock veins are black and linear, veined, or cystic under the microscope. The width of the veins varies from micron to millimeter.

In most L ordinary chondrites that were affected by intense shock metamorphism, the shock melting veins are dominated by molten silicate minerals. The mineral compositions and the structure of the veins significantly differ from those of the metal-sulfide veins. Different from the H ordinary chondrites, the width of the silicate melt veins ranges from tens of microns to several millimeters. The veins are mainly composed of matrix and coarse-grained silicate. In widely spaced melt veins (width > 100 μm), silicate mineral fragments account for about 50%–70% vol% of the melt. In contrast, the fine shock veins or vesicles with a width of only tens of microns are mainly composed of very fine matrix, and the portion of fragments accounts for less than 10% vol% of the melt.

In a shock vein of sample GRV 090463, several mineral fragments with bright gray margins and dark gray cores are recognized by the BSE image (Figure 5). EPMA analysis identifies both domains as olivine. However, the iron content is significantly higher in the bright gray margins than in the dark gray core. Laser Raman spectrum analysis shows two main peaks, near 795 cm^{-1} and 840 cm^{-1}, for the bright gray margins, which are typical peaks of ringwoodite (Figure 6). The dark gray core records two main peaks, near 820 cm^{-1} and 850 cm^{-1}, which are characteristic for olivine. Moreover, we analyzed the fine silicate grains in the shock melting veins with laser Raman spectroscopy. These grains record characteristic peaks at 925 cm^{-1}, 652 cm^{-1}, and 589 cm^{-1}, identifying them as majorite–pyrope solid solutions that crystallized from the silicate melt at high temperatures and high pressures [26,27]. EPMA analysis document that the Cr_2O_3 (0.45%) and CaO (1.43%) contents in the majorite–pyrope solid solution are higher than in low-Ca pyroxene (enstatite) (Cr_2O_3: 0.16%; CaO: 0.94%).
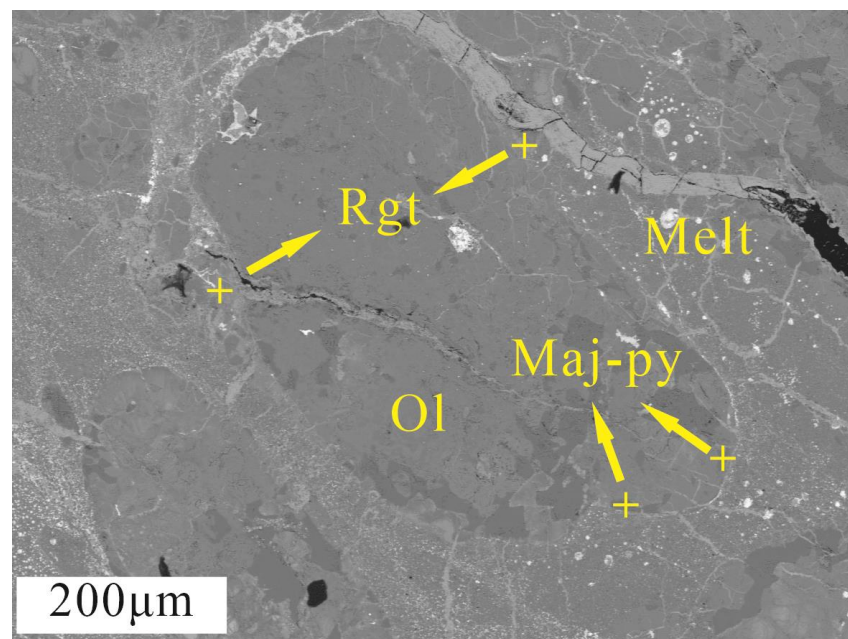
Figure 5. BSE images of ringwoodite and majorite-pyrope in sample GRV 090463. Rgt—ringwoodite; Maj-py—majorite-pyrope.
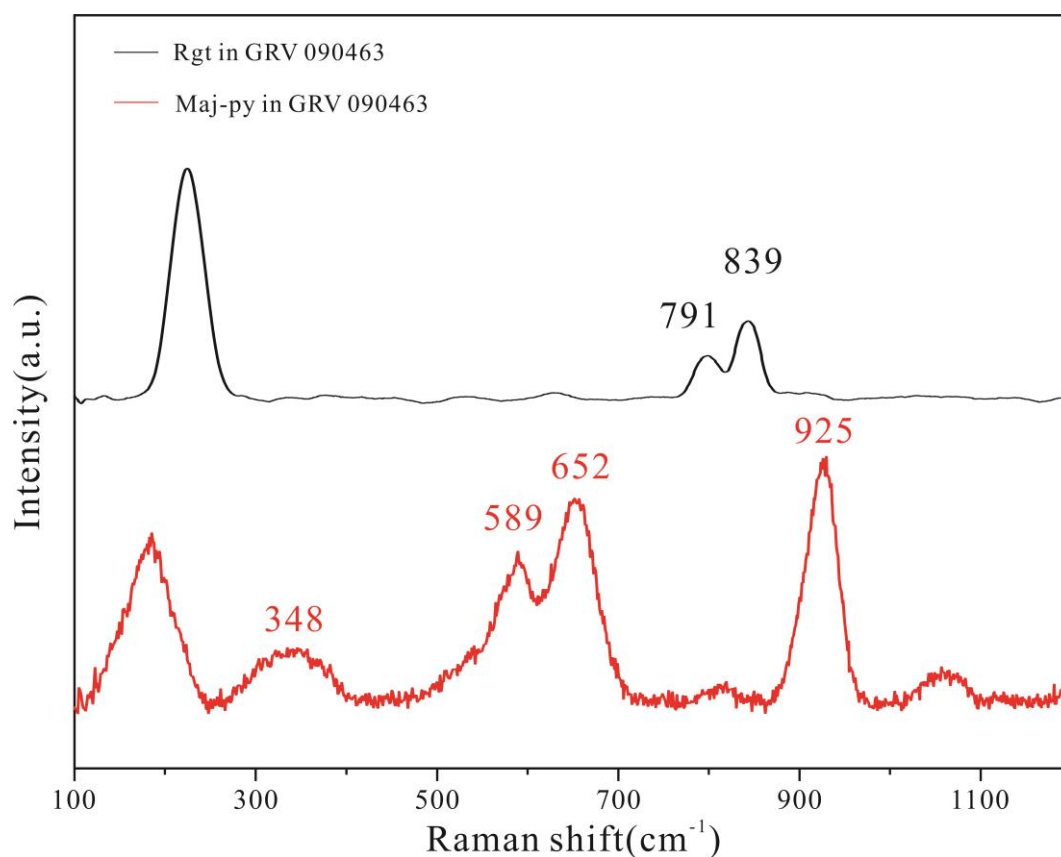
Figure 6. Raman spectra of ringwoodite (black) and majorite–pyrope (red) in GRV 090463.

4. Discussion

Considering that the weathering in meteorites is mainly reflected in secondary minerals and metal oxides, it will not destroy the Raman peaks of olivine and pyroxene [28]. From the huge difference in Figure 4, it is not difficult to determine that the olivine and pyroxene data from RRUFF have good regularity, but the sample data selected in this paper have poor correlation. The weak correlations in meteorite data may be related to the low number of samples in the available databases causing high sensitivity of the fitting curve. Second, due to the restricted distribution range of the chemical groups of ordinary chondrites and the high required precision, some acceptable errors in the full range may affect the fitting. Third, it may be that the olivine and pyroxene stored in the RRUFF database have good crystallinity and pure composition, while the crystal structure and chemical composition of the minerals have changed to varying degrees after the parent body of the sample selected in this paper was affected by external influences [29].

The rise of the full width at half maximum (FWHM) of the Raman peak is correlated with an increase of the amorphization degree of the material [30]. Part of the minerals melted during the impact of the meteorite, resulting in a disordered crystal structure and a decrease in the crystallinity [31]. Therefore, we propose a good correlation between FWHM in the Raman spectrum and the shock displacement [32]. The average Raman spectral FWHM of olivine in the 16 investigated meteorite samples was about 14–16 cm^{-1}. In sample GRV 090521, it reaches the highest value with >20 cm^{-1}. In contrast, the FWHM of the well-crystallized olivine in the earth is generally below 10 cm^{-1} [30]. The FWHM of the Raman spectrum of the detected ringwoodite is about 20 cm^{-1}, thus it is higher than that of olivine in the same sample.

Since the mineral characteristic peak (FWHM) is affected by the shock degree, samples GRV 090403, GRV 090421, GRV 090511, and GRV 090517, as well as samples S2 and S4 are compared with the half peak width of olivine and pyroxene in different positions (Table 3).

Table 3 documents that the FWHM of the Raman spectrum with the melt is wider than that with the matrix in the same strongly shocked sample. In contrast, in samples with low shock degrees, the FWHM of the minerals show no significant changes. However, this link is probably only a qualitative relationship. Although a difference between the mineral Raman half peak width of the matrix in the same sample is observed, a quantification of the relationship remains uncertain. The possible applicability of the half peak width of the meteorite minerals to determine the shock pressure requires additional experimental studies. We conducted Raman analyses on the minerals on both sides of the melt of some samples, and the results show that the closer the distance to the melt, the wider the FWHM of the minerals, and the centroid of Raman peaks also change. For example, in GRV 090511, which was received outside the greater part of the shock, the position of pyroxene Peak C and the FWHM are larger (Figure 7).

Table 3. Comparison of the FWHM of the Raman spectra of minerals in different positions of selected samples.

Mineral	Number	Shock Stage	Position	FWHM in Peak A	FWHM in Peak B	FWHM in Peak C
Ol	GRV 090403	S2	matrix	10.33 11.01	13.64 14.66	
	GRV 090421	S2	matrix	10.63 12.22	13.52 15.40	
	GRV 090511	S4	matrix shock vein	14.40 16.09	16.13 17.47	
	GRV 090517	S4	matrix shock vein	11.83 13.29	14.77 16.01	
Px	GRV 090403	S2	matrix	12.21 15.35	13.07 11.46	13.19 20.07
	GRV 090421	S2	matrix	11.08 12.21	12.23 12.90	13.50 22.73
	GRV 090511	S4	matrix shock vein	14.99 30.95	15.87 21.94	16.99 24.05
	GRV 090517	S4	matrix shock vein	16.17 17.12	13.24 15.50	17.66 22.90

According to the Raman spectra of pyroxene at different positions, it can be concluded that with the increase of pressure, the Raman characteristic peak of pyroxene shifts in the direction of a high wavenumber, and the value of FWHM increases, and the wave number of the Raman characteristic peak of pyroxene may not be linear with the change of pressure. For olivine, the same result exists. Foster [33] and Harris [34] found that with increasing pressure, the wavenumber and FWHM of the olivine Raman characteristic double peaks increased, and the wavenumber difference between the two Raman peaks decreased. Due to the influence of the impact effect on the Raman spectra of pyroxene, it can be explained that the experimental data in this paper show that the correspondence between the chemical composition of olivine and pyroxene and the Raman peak positions are inconsistent with previous studies. This further shows that the Raman spectra of olivine and pyroxene in common chondrites are affected by both composition and impact effects, and it is unreliable to expect to use a single index to classify them. For this reason, Harris argues that Kuebler's determination of olivine by Raman spectra alone does not rule out impact in 2006 [34].
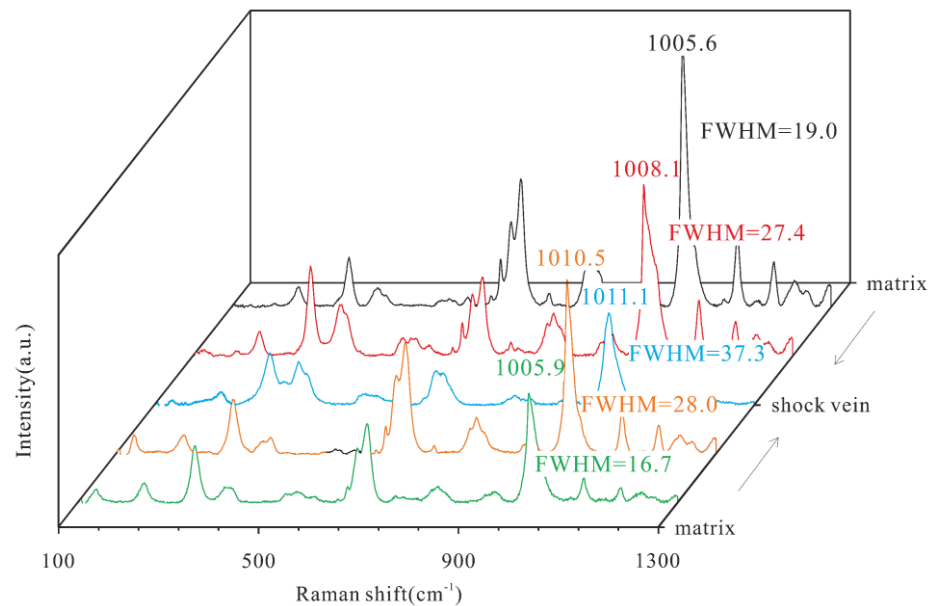
Figure 7. The Raman spectrum of olivine at different position in GRV 090511.

Ordinary chondrites generally discriminate shock degree according to the high-pressure minerals. Very fine-grained high-pressure minerals are widely distributed in the melt pockets, interconnecting melt veins and opaque shock veins, but are easily overlooked in the polarizing microscope due to the fine grain size. Therefore, the existing classification standards for judging the shock stage based on characteristic high-pressure minerals are easily affected. Electron probe microanalysis (EPMA) is the most precise instrument for the quantitative chemical analysis of the characteristic high-pressure minerals, including ringwoodite and majorite, and is thus the best way to constrain the degree of shock metamorphism. However, these analyses are time-consuming. Laser Raman technology is the most appropriate method if the high-pressure minerals must be analyzed qualitatively and rapidly (several seconds to tens of seconds). For example, sample GRV 090463 was grouped into S4 in the previous classification. However, it should be classified as S6 according to the high-pressure minerals such as ringwoodite and majorite that we detected in the shock veins by Raman spectroscopy. Such incorrect classification, exemplified by GRV 090463, is ubiquitous. The example substantiates that the application of laser Raman technology for the detection of the high-pressure minerals in the meteorite samples should be preconditioned to constrain to the shock grade of the meteorite, and hence the accuracy of the classification would be significantly improved.

5. Conclusions

We studied the correlation between the characteristic Raman peaks of olivine and pyroxene and the content of iron in balanced ordinary chondrites. Although this correlation is obvious in the characteristic peaks of olivine between 800–856 cm^{-1} and pyroxene between 675–680 cm^{-1}, due to the low accuracy, this correlation can only be regarded as an ordinary chondrite, and so this correlation can only be used as a reference for the preliminary chemical group classification of ordinary chondrites.

Shock events can influence the FWHM of the Raman spectrum of minerals in ordinary chondrites, and a positive correlation between them may occur.

Micro-Raman analysis is a quick and effective method to detect characteristic high-pressure minerals in meteorite samples. Therefore, we suggest the use of Raman spectroscopy, in combination with polarizing microscope and subsequent EPMA analysis, to classify the degree of shock metamorphism of ordinary chondrites and to check previous classifications.

Appendix A

Table A1. The Raman spectrum and corresponding EPMA data of olivine in selected samples.

Sample	Number	Peak A/cm^{-1}	FWHM/cm^{-1}	Peak B/cm^{-1}	FWHM/cm^{-1}	Fa/mol%	av.Fa/mol%
GRV 090360	1	820.9	11.7	852.9	15.6	25.7	
	2	821.0	13.3	852.0	16.5	26.0	
	3	821.5	11.6	852.2	15.4	25.6	
	4	818.9	16.0	850.4	18.0	25.2	
	5	819.4	13.9	851.0	16.6	25.3	
	6	821.8	14.6	853.4	17.0	25.8	
	7	821.0	14.4	852.7	17.0	25.3	
	8	821.4	15.7	852.7	17.3	25.1	
	9	821.9	15.5	851.8	15.9	25.2	
	10	821.0	16.3	852.9	14.9	25.7	22.1 (n = 10)
GRV 090361	1	820.3	16.6	850.2	16.4	25.5	
	2	819.5	15.0	849.7	18.0	24.6	
	3	820.1	15.6	849.3	20.6	25.1	
	4	819.3	15.9	849.6	17.2	26.0	
	5	819.7	16.8	852.5	17.4	24.6	
	6	820.6	15.9	851.9	15.4	25.6	
	7	819.7	16.8	851.6	14.2	24.7	
	8	820.7	13.3	850.8	14.0	25.3	
	9	821.0	16.9	852.8	15.5	25.3	
	10	821.1	14.7	850.1	16.1	25.2	21.4 (n = 10)
363	1	820.7	13.0	850.5	17.3	25.0	
	2	820.6	13.1	851.8	16.4	25.3	
	3	820.7	13.1	850.8	16.5	25.1	
	4	820.3	13.2	851.6	16.4	25.6	
	5	820.3	12.0	851.7	15.6	25.4	
	6	820.3	13.3	852.9	16.2	25.4	
	7	819.1	10.1	851.7	14.7	24.6	
	8	820.4	11.8	851.9	17.0	25.5	
	9	821.9	11.9	851.1	17.3	24.6	
	10	820.0	13.7	850.6	15.6	25.4	21.8 (n = 10)

Table A1. *Cont.*

Sample	Number	Peak A/cm^{-1}	FWHM/cm^{-1}	Peak B/cm^{-1}	FWHM/cm^{-1}	Fa/mol%	av.Fa/mol%
GRV 090376	1	820.7	11.9	851.6	15.8	25.2	
	2	820.5	14.8	850.6	17.2	25.3	
	3	821.0	13.2	851.3	16.5	24.9	
	4	820.3	13.5	851.6	16.7	25.6	
	5	820.9	13.0	851.4	15.9	24.9	
	6	821.3	12.3	851.1	13.4	25.3	
	7	821.2	10.8	851.7	15.9	25.5	
	8	821.1	11.1	850.5	16.2	25.2	
	9	821.0	11.6	852.6	14.5	25.5	
	10	821.6	10.8	852.4	15.3	25.7	21.3 (n =10)
GRV 090379	1	820.6	13.3	851.7	16.5	25.5	
	2	820.7	11.2	852.0	14.0	25.1	
	3	820.5	10.9	851.8	14.6	25.9	
	4	820.6	12.5	852.1	16.5	25.3	
	5	821.2	12.6	853.0	14.1	25.1	
	6	821.5	11.6	852.5	14.8	25.0	
	7	819.9	11.9	850.7	13.1	24.5	
	8	820.6	12.1	851.2	14.2	25.8	
	9	821.2	10.2	852.4	16.1	25.0	
	10	819.9	10.8	852.8	14.3	24.8	21.3 (n = 10)
GRV 090380	1	820.6	12.5	851.3	15.3	24.7	
	2	819.9	14.4	850.7	17.0	25.2	
	3	820.7	13.1	851.3	16.1	24.7	
	4	820.0	15.2	850.1	18.0	25.1	
	5	820.3	13.0	851.4	16.2	24.7	
	6	821.6	13.6	850.4	17.4	25.0	
	7	820.4	13.5	850.2	16.6	25.5	
	8	819.3	12.0	852.1	16.0	26.0	
	9	821.0	11.8	852.9	16.7	25.5	
	10	819.2	13.7	851.4	15.1	24.5	21.6 (n = 10)
GRV 090403	1	821.1	10.6	852.5	14.1	20.1	
	2	821.0	11.0	852.7	14.7	20.5	
	3	821.2	10.7	852.9	13.4	19.9	
	4	821.3	10.6	853.1	13.6	19.9	
	5	822.0	10.3	853.3	13.6	19.9	
	6	821.5	10.6	853.5	14.1	20.0	
	7	819.1	10.5	853.9	15.3	19.9	
	8	821.7	12.4	853.7	15.7	19.8	
	9	819.9	12.6	853.5	14.1	19.9	
	10	820.3	10.7	853.1	16.1	19.8	17.7 (n = 10)
GRV 090421	1	820.7	11.0	851.9	14.9	19.4	
	2	820.7	12.2	852.0	15.4	19.4	
	3	821.0	10.6	852.4	13.5	19.2	
	4	820.9	11.6	852.1	14.1	19.3	
	5	821.4	13.8	852.9	14.6	19.4	
	6	821.2	11.9	853.9	15.2	19.3	
	7	820.2	11.4	852.9	14.5	19.1	
	8	819.7	12.3	853.3	14.3	19.2	
	9	822.0	10.7	853.7	16.4	19.2	
	10	820.8	12.1	852.7	15.1	19.5	16.9 (n = 10)
GRV 090463	1	821.0	13.3	852.4	16.8	24.1	
	2	820.3	13.7	850.0	17.1	25.4	
	3	820.9	16.1	851.0	17.5	24.7	
	4	820.9	14.6	851.1	17.2	24.8	
	5	820.7	12.9	853.2	17.1	25.8	

Table A1. *Cont.*

Sample	Number	Peak A/cm^{-1}	FWHM/cm^{-1}	Peak B/cm^{-1}	FWHM/cm^{-1}	Fa/mol%	av.Fa/mol%
	6	821.2	11.7	851.9	14.9	24.8	
	7	820.3	10.5	852.1	14.8	24.6	
	8	821.1	10.9	851.9	14.7	24.9	
	9	820.7	11.7	852.4	16.1	24.9	
	10	819.9	14.0	852.0	16.4	25.3	22(n = 10)
	1	820.7	11.9	851.2	16.8	24.9	
	2	819.8	13.8	850.9	16.9	25.3	
	3	820.8	11.6	851.4	15.3	24.9	
	4	820.3	12.3	850.9	15.6	25.0	
	5	820.6	11.4	851.0	14.7	25.0	
GRV 090448	6	819.7	10.3	851.7	15.5	26.0	
	7	820.2	11.6	852.7	14.7	24.7	
	8	819.8	11.1	850.8	14.1	25.0	
	9	820.1	12.6	852.6	14.7	25.5	
	10	820.0	11.3	851.5	14.5	24.9	21.1 (n = 10)
	1	820.1	13.3	851.4	16.0	25.1	
	2	820.4	12.2	850.8	15.8	24.9	
	3	820.1	11.8	851.3	15.8	25.6	
	4	820.3	12.4	851.2	15.4	25.1	
	5	819.2	10.4	852.5	16.8	25.2	
GRV 090449	6	821.3	12.4	850.1	14.2	25.4	
	7	820.6	11.2	851.1	13.3	25.8	
	8	820.7	13.7	851.4	16.9	25.6	
	9	820.4	11.9	851.4	16.5	24.6	
	10	819.1	11.3	850.7	16.0	25.8	22 (n = 10)
	1	820.7	14.0	850.3	17.2	25.0	
	2	821.2	14.4	851.4	16.1	26.1	
	3	820.9	14.8	851.2	16.5	25.3	
	4	820.8	15.4	851.0	16.8	25.1	
	5	821.1	13.8	851.9	17.5	24.8	
GRV 090511	6	821.2	15.7	850.8	17.2	24.5	
	7	820.0	15.1	850.1	16.6	25.1	
	8	821.5	14.4	850.5	15.2	25.3	
	9	819.5	15.4	852.9	14.9	25.6	
	10	820.9	14.1	852.5	15.7	24.9	21.3 (n = 10)
	1	820.7	13.3	851.9	16.1	25.3	
	2	821.1	11.8	852.6	14.8	24.8	
	3	820.6	12.1	851.8	15.4	25.7	
	4	820.2	13.3	851.8	16.0	25.7	
	5	819.6	11.8	851.9	14.1	25.3	
GRV 090517	6	820.6	12.2	852.3	16.9	25.1	
	7	820.2	13.8	852.7	14.5	25.6	
	8	819.6	12.3	852.2	16.4	25.2	
	9	820.7	13.9	850.8	13.1	25.7	
	10	820.4	11.1	851.1	13.4	24.9	21.5 (n = 10)
	1	820.2	18.3	851.4	21.8	25.1	
	2	819.0	19.8	850.6	23.7	26.4	
	3	819.8	18.0	850.6	23.7	26.3	
	4	818.9	24.1	851.1	22.8	26.6	
	5	820.3	19.6	851.6	21.1	24.8	
GRV 090519	6	821.8	15.3	850.6	23.2	24.5	
	7	819.5	14.2	850.9	20.8	24.8	
	8	819.4	15.6	851.2	22.7	24.6	
	9	820.2	15.1	852.2	20.8	25.0	
	10	821.1	13.6	852.9	20.9	25.6	
	11	819.7	15.5	852.2	20.5	25.7	21.5 (n = 10)

Table A1. *Cont.*

Sample	Number	Peak A/cm^{-1}	FWHM/cm^{-1}	Peak B/cm^{-1}	FWHM/cm^{-1}	Fa/mol%	av.Fa/mol%
GRV 090520	1	820.2	14.4	851.7	17.8	25.3	
	2	819.3	14.8	851.1	18.2	25.2	
	3	820.3	13.2	851.5	16.8	25.1	
	4	820.1	13.9	850.6	17.3	24.7	
	5	820.3	15.5	850.2	17.0	24.6	
	6	820.6	15.0	851.2	16.3	25.8	
	7	819.9	13.8	850.2	16.5	25.0	
	8	820.0	13.9	852.5	17.2	25.1	
	9	822.0	14.3	851.1	17.5	24.7	
	10	820.8	13.2	850.1	17.3	25.2	21.4 (n = 10)
GRV 090521	1	819.8	22.4	851.0	23.1	24.3	
	2	819.8	22.3	851.0	23.4	25.0	
	3	820.3	24.0	851.2	21.4	25.5	
	4	820.3	24.3	851.3	21.6	25.5	
	5	820.9	20.7	851.6	20.1	25.5	
	6	822.0	23.1	851.2	22.9	25.7	
	7	820.8	20.9	852.1	22.0	24.7	
	8	821.4	24.2	851.9	21.7	25.4	
	9	822.0	20.4	850.0	23.4	24.6	
	10	820.5	22.3	852.8	22.4	25.6	21.6 (n = 10)

Note: Fa = Fe/(Fe+Mg) molar × 100. The Raman spectral data of the test point correspond to the EPMA data. Av.Fa is the average of all EPMA data. n is the number of EPMA analysis. Standard deviation less than 0.001.

Table A2. The Raman spectrum and corresponding EPMA data of pyroxene in selected samples.

Sample	Number	Peak A/cm^{-1}	FWHM/cm^{-1}	Peak B/cm^{-1}	FWHM/cm^{-1}	Peak C/cm^{-1}	FWHM/cm^{-1}	Fs/mol%	av.Fs/mol%
GRV 090360	1	337.0	14.1	679.6	14.1	1009.6	21.3	21.9	
	2	336.4	17.5	679.5	17.5	1011.4	24.7	22.1	
	3	336.5	11.7	679.1	11.7	1013.6	27.1	22.5	
	4	335.9	12.5	678.8	14.1	1008.6	15.1	22.0	
	5	335.3	16.9	678.9	16.3	1011.2	24.7	21.9	
	6	334.0	16.0	677.5	15.3	1008.4	13.9	21.9	
	7	334.3	14.7	679.2	16.2	1010.3	21.9	22.0	
	8	334.4	14.7	679.2	14.4	1011.9	27.5	22.0	
	9	335.9	15.5	679.6	13.9	1009.6	18.5	22.2	
	10	334.8	15.4	678.0	16.8	1009.2	17.2	22.0	22.1 (n = 10)
GRV 090361	1	333.6	12.9	677.2	15.6	1008.5	23.7	23.0	
	2	334.4	13.7	677.5	12.7	1005.5	14.8	21.3	
	3	334.2	14.2	677.5	12.3	1005.2	16.5	21.5	
	4	335.9	7.0	678.1	12.1	1005.0	13.3	21.2	
	5	335.7	12.8	677.1	18.0	1011.9	27.6	21.3	
	6	334.9	13.8	680.0	16.2	1009.6	19.7	21.5	
	7	335.7	14.2	678.4	14.8	1011.0	23.6	21.4	
	8	335.4	12.5	679.2	15.8	1011.9	27.6	21.1	
	9	335.0	13.2	678.5	11.8	1008.8	15.7	21.1	
	10	335.2	12.0	677.3	13.0	1009.6	18.7	21.4	21.4 (n = 10)
GRV 090363	1	334.7	20.9	679.6	20.9	1010.1	24.0	22.5	
	2	334.9	13.5	679.4	17.1	1010.5	24.9	22.1	
	3	336.0	12.4	678.3	11.9	1010.5	24.7	21.6	
	4	336.0	12.1	679.8	12.7	1006.1	13.8	20.9	
	5	335.5	14.7	678.6	16.3	1011.9	27.9	21.5	
	6	334.2	12.1	677.7	14.3	1010.2	20.9	21.6	
	7	335.2	12.2	679.3	16.9	1011.3	25.8	22.0	
	8	334.1	14.7	679.1	16.7	1010.9	23.1	21.5	

Table A2. *Cont.*

Sample	Number	Peak A/cm^{-1}	FWHM/cm^{-1}	Peak B/cm^{-1}	FWHM/cm^{-1}	Peak C/cm^{-1}	FWHM/cm^{-1}	Fs/mol%	av.Fs/mol%
	9	334.7	12.6	677.2	15.1	1008.4	14.8	22.0	
	10	334.8	12.3	677.1	16.9	1008.6	15.1	21.6	21.8 (n = 10)
	1	336.9	13.6	679.5	12.5	1008.3	18.7	20.4	
	2	334.0	15.3	678.5	20.9	1006.5	18.3	22.3	
	3	334.8	15.3	678.3	13.4	1006.2	15.2	21.4	
	4	335.4	14.4	678.3	16.6	1007.9	13.9	21.1	
GRV	5	335.2	13.4	679.4	14.3	1010.7	22.5	21.0	
090376	6	334.2	13.6	677.7	14.8	1008.0	13.1	21.4	
	7	334.8	13.0	679.5	15.9	1010.8	22.7	21.1	
	8	334.9	13.0	679.9	16.4	1011.2	24.9	21.2	
	9	335.9	13.1	677.0	17.0	1008.1	13.5	21.4	
	10	334.1	12.6	680.0	15.7	1007.0	13.4	21.1	21.3 (n = 10)
	1	336.8	11.6	679.2	13.8	1008.0	17.5	21.8	
	2	334.3	13.0	678.6	12.8	1007.1	20.2	21.0	
	3	334.9	12.5	678.2	12.7	1005.6	13.1	21.0	
	4	334.1	14.6	679.8	11.7	1008.4	14.9	21.3	
GRV	5	335.3	13.0	677.9	14.7	1010.1	20.5	21.4	
090379	6	334.8	12.0	677.2	12.7	1009.6	19.9	21.2	
	7	335.6	13.6	677.2	11.0	1009.3	19.4	21.4	
	8	334.0	13.6	678.2	13.8	1010.7	22.5	21.2	
	9	334.8	13.5	677.2	11.6	1009.0	17.0	21.1	
	10	334.0	13.7	678.3	12.2	1006.1	13.2	21.5	21.3 (n = 10)
	1	336.0	13.8	678.5	12.5	1006.6	15.6	22.9	
	2	335.6	14.4	678.3	16.1	1009.8	22.0	21.7	
	3	333.3	17.7	677.7	19.8	1005.9	17.7	20.8	
	4	335.6	14.6	677.1	15.2	1011.3	25.3	21.8	
GRV	5	335.1	12.8	678.4	15.6	1008.4	14.6	21.4	
090380	6	335.0	14.8	677.8	14.4	1010.3	21.8	21.6	
	7	335.5	13.9	679.6	15.8	1010.7	22.4	21.6	
	8	335.6	14.2	680.0	14.1	1009.6	19.0	21.5	
	9	335.0	12.3	677.1	16.4	1009.3	17.8	21.7	
	10	334.7	13.5	678.4	16.3	1008.9	16.0	21.4	21.6 (n = 10)
	1	337.3	11.4	679.9	12.2	1008.3	17.0	17.7	
	2	337.4	15.4	679.8	11.5	1009.5	20.1	17.6	
	3	337.2	12.2	680.1	13.1	1007.4	13.2	18.0	
	4	337.7	11.4	680.4	13.2	1008.8	17.2	17.6	
GRV	5	338.1	11.9	680.5	12.3	1013.0	25.3	17.4	
090403	6	337.3	12.5	680.4	17.9	1009.7	20.0	17.9	
	7	336.9	13.7	679.6	14.7	1009.0	16.9	17.8	
	8	336.4	13.3	680.5	16.7	1009.3	18.0	17.9	
	9	337.4	14.6	680.2	18.2	1010.6	22.4	17.7	
	10	336.3	14.9	679.6	16.0	1010.1	20.5	17.7	17.7 (n = 10)
	1	336.2	13.3	679.4	12.2	1006.6	14.2	17.1	
	2	336.5	12.2	679.8	12.9	1011.9	22.7	17.0	
	3	336.3	11.8	679.8	20.5	1006.3	19.5	17.0	
	4	337.3	25.4	679.3	12.4	1007.5	14.7	16.5	
GRV	5	337.0	11.1	679.9	12.2	1006.4	13.5	16.8	
090421	6	336.7	13.0	680.0	12.2	1004.3	12.9	17.0	
	7	336.5	13.7	679.8	16.7	1007.2	13.6	17.1	
	8	337.6	12.8	679.7	14.7	1006.6	13.4	16.9	
	9	336.9	14.9	680.0	11.5	1007.0	13.5	17.0	
	10	337.8	13.0	680.2	13.6	1006.9	13.4	17.2	16.9 (n = 10)
GRV	1	335.0	17.4	680.5	24.9	1010.1	22.3	22.0	
090463	2	337.5	48.4	679.4	16.2	1008.0	20.7	21.3	
	3	336.0	13.9	680.6	17.7	1010.2	26.3	21.6	

Table A2. *Cont.*

Sample	Number	Peak A/cm^{-1}	FWHM/cm^{-1}	Peak B/cm^{-1}	FWHM/cm^{-1}	Peak C/cm^{-1}	FWHM/cm^{-1}	Fs/mol%	av.Fs/mol%
	4	337.9	34.7	680.4	16.8	1013.0	27.5	21.2	
	5	335.9	18.7	678.2	16.3	1009.4	18.4	22.0	
	6	335.9	19.6	679.3	15.0	1009.7	20.3	22.1	
	7	335.4	21.2	678.5	17.0	1009.9	20.3	22.1	
	8	335.8	18.7	678.9	12.5	1010.5	22.1	22.1	
	9	335.6	21.5	679.7	16.6	1008.9	15.8	21.8	
	10	334.8	20.7	678.5	17.9	1007.8	13.8	21.9	22.0 (n = 10)
	1	335.9	12.5	679.2	12.6	1007.7	18.4	20.7	
	2	335.1	14.1	678.9	13.8	1008.2	18.8	21.7	
	3	335.7	13.6	678.5	12.5	1007.0	16.7	20.9	
	4	334.9	13.6	678.0	13.7	1006.2	13.3	21.8	
GRV	5	335.8	13.0	678.4	12.4	1008.4	14.2	22.1	
090448	6	334.5	13.8	678.1	13.4	1011.0	23.8	21.2	
	7	334.2	14.4	679.3	12.9	1008.5	15.0	21.0	
	8	335.2	14.8	679.1	12.3	1008.1	13.1	21.0	
	9	334.6	14.1	680.0	18.4	1009.4	18.1	20.9	
	10	335.5	15.8	679.1	17.2	1010.2	24.1	20.8	21.1 (n = 10)
	1	334.7	19.3	677.6	13.1	1009.5	24.3	22.6	
	2	335.7	15.3	678.6	16.3	1011.3	24.1	21.9	
	3	335.8	14.8	678.3	18.4	1010.6	29.0	21.8	
	4	335.6	14.0	679.1	25.9	1011.4	25.2	22.1	
GRV	5	336.6	29.3	678.7	17.3	1012.2	27.0	21.6	
090449	6	335.4	17.1	677.6	17.3	1003.3	12.0	22.1	
	7	334.0	16.3	678.9	14.1	1005.4	13.0	22.1	
	8	335.2	16.8	677.5	17.0	1003.9	12.7	22.2	
	9	335.8	18.2	679.1	17.2	1003.1	12.0	22.1	
	10	335.3	14.6	679.6	12.5	1005.8	13.2	22.2	22.0 (n = 10)
	1	334.6	15.4	678.6	15.1	1003.6	12.1	21.2	
	2	334.5	15.0	679.1	15.9	1005.4	17.0	21.4	
	3	331.6	31.0	679.9	21.9	1010.2	24.1	21.6	
	4	336.3	14.8	674.6	25.7	1003.4	9.4	20.8	
GRV	5	335.5	12.3	679.7	13.2	1005.7	14.9	21.1	
090511	6	335.1	14.8	679.7	14.2	1003.5	12.2	21.3	
	7	334.0	14.9	679.3	14.2	1003.2	12.0	21.0	
	8	335.6	15.8	678.0	14.4	1005.8	13.2	21.2	
	9	336.0	16.7	679.7	16.9	1007.1	13.6	21.3	
	10	335.7	15.3	679.7	15.7	1007.2	13.8	21.2	21.3 (n = 10)
	1	336.2	17.1	679.3	16.5	1012.2	32.1	21.0	
	2	334.5	16.2	678.7	13.2	1006.6	17.7	21.6	
	3	334.7	17.1	678.7	15.5	1009.2	22.9	21.6	
	4	335.6	15.8	677.3	16.4	1008.8	15.2	21.6	
GRV	5	335.5	16.8	678.2	16.8	1011.3	25.2	21.4	
090517	6	334.5	16.9	677.7	17.0	1009.3	17.5	21.5	
	7	334.2	16.2	679.6	14.3	1008.9	16.2	21.3	
	8	336.0	17.0	678.9	14.5	1011.3	25.6	21.6	
	9	335.6	16.1	677.3	14.9	1011.0	24.2	21.6	
	10	334.7	15.8	677.8	15.9	1008.0	14.0	21.3	21.5 (n = 10)
	1	333.4	19.5	677.3	27.1	1007.8	27.4	21.2	
	2	334.6	22.3	678.1	23.2	1013.7	37.6	21.0	
GRV	3	335.2	21.2	678.4	24.0	1006.7	13.4	21.1	
090519	4	334.9	19.7	678.5	20.9	1010.4	22.0	21.9	
	5	334.4	21.7	679.6	20.1	1009.6	19.9	21.8	
	6	334.3	21.4	679.1	24.6	1010.2	21.1	21.3	
	7	336.0	21.0	678.4	21.7	1010.3	21.8	21.2	

Table A2. *Cont.*

Sample	Number	Peak A/cm^{-1}	FWHM/cm^{-1}	Peak B/cm^{-1}	FWHM/cm^{-1}	Peak C/cm^{-1}	FWHM/cm^{-1}	Fs/mol%	av.Fs/mol%
	8	334.3	22.7	677.8	21.7	1011.4	26.0	21.9	
	9	334.9	22.5	678.7	23.4	1011.1	24.2	21.6	
	10	334.1	19.8	679.2	24.3	1011.7	26.6	21.5	21.5 (n = 10)
	1	335.8	23.9	680.3	18.6	1008.1	30.0	20.6	
	2	333.3	24.6	678.7	21.7	1010.4	35.0	21.2	
	3	332.8	32.8	677.9	15.4	1005.1	18.5	22.8	
	4	335.1	19.7	677.5	13.4	1006.3	13.3	20.6	
GRV 090520	5	335.7	20.3	679.3	12.8	1008.9	16.7	21.1	
	6	335.3	22.0	679.6	16.5	1008.3	13.9	21.1	
	7	335.1	20.8	678.6	16.6	1009.1	17.1	20.5	
	8	335.9	22.2	677.5	14.0	1008.4	14.1	20.9	
	9	335.4	18.4	679.7	15.1	1009.5	18.5	21.1	
	10	335.8	20.4	679.4	18.6	1011.3	25.0	21.3	21.0 (n = 10)
	1	332.7	23.0	676.7	18.1	1005.3	17.7	21.9	
	2	332.5	23.3	675.2	31.9	1004.2	23.3	22.8	
	3	335.1	18.0	676.3	24.7	1002.7	11.8	20.8	
	4	332.6	19.5	675.8	24.2	1003.6	17.1	22.0	
GRV 090521	5	334.0	20.9	679.5	22.7	1003.9	12.6	21.4	
	6	334.9	21.4	679.8	25.8	1005.5	13.0	21.1	
	7	334.6	19.0	678.4	25.3	1004.4	12.9	21.3	
	8	335.7	18.2	677.3	20.9	1003.4	12.1	21.1	
	9	335.0	21.0	678.5	22.4	1004.9	12.9	21.4	
	10	335.3	18.1	679.0	21.5	1006.0	13.2	20.9	21.6 (n = 10)

Note: Fs = Fe/(Fe + Mg + Ca) molar $\times$ 100. The Raman spectral data of the test point correspond to the EPMA data. Av.Fs is the average of all EPMA data. n is the number of EPMA analysis. Standard deviation less than 0.001.

References

1. Hutchison, R. *Meteorites: A Petrologic, Chemical and Isotopic Synthesis*; Cambridge University Press: Cambridge, UK, 2006.
2. Miao, B.; Xia, Z.; Zhang, C.; Ou, R.; Sun, Y. Progress of Antarctic meteorite survey and research in China. *Adv. Polar Sci.* **2018**, *29*, 61–77.
3. Xia, Z.; Zhang, J.; Miao, B.; Ou, R.; Xie, L.; Yang, R.; Jing, Y. Meteorite classification for building the Chinese Antarctic Meteorite Depository—Introduction of the classification of 500 grove mountains meteorites. *Adv. Polar Sci.* **2016**, *27*, 56–63.
4. Van Schmus, W.; Wood, J.A. A chemical-petrologic classification for the chondritic meteorites. *Geochim. Et Cosmochim. Acta* **1967**, *31*, 747–765. [CrossRef]
5. Grossman, J.; Rubin, A. White paper report for the Nomenclature Committee on the composition of olivine and pyroxene in equilibrated ordinary chondrites. Unpublished work. 2006. Available online: https://www.lpi.usra.edu/meteor/docs/whitepaper.pdf (accessed on 13 July 2022).
6. Wasson, J.T.; Kallemeyn, G.W. Compositions of chondrites. *Philos. Trans. R. Soc. London. Ser. A Math. Phys. Sci.* **1988**, *325*, 535–544.
7. Baryshnikova, G.; Lavrukhina, A. The classification of the chondrules of ordinary chondrites. *Geokhimiia* **1982**, *58*, 490–503.
8. Rochette, P.; Sagnotti, L.; Bourot-Denise, M.; Consolmagno, G.; Folco, L.; Gattacceca, J.; Osete, M.L.; Pesonen, L. Magnetic classification of stony meteorites: 1. Ordinary chondrites. *Meteorit. Planet. Sci.* **2003**, *38*, 251–268. [CrossRef]
9. Tomioka, N.; Miyahara, M. High-pressure minerals in shocked meteorites. *Meteorit. Planet. Sci.* **2017**, *52*, 2017–2039. [CrossRef]
10. Rubin, A.E. Mineralogy of meteorite groups. *Meteorit. Planet. Sci.* **1997**, *32*, 231–247. [CrossRef]
11. Fritz, J.; Greshake, A.; Fernandes, V.A. Revising the shock classification of meteorites. *Meteorit. Planet. Sci.* **2017**, *52*, 1216–1232. [CrossRef]
12. Sharp, T.G.; DeCarli, P.S. Shock effects in meteorites. *Meteor. Early Sol. Syst. II* **2006**, *943*, 653–677.
13. Stöffler, D.; Keil, K.; RD, S.E. Shock metamorphism of ordinary chondrites. *Geochim. Et Cosmochim. Acta* **1991**, *55*, 3845–3867. [CrossRef]
14. Angel, S.M.; Gomer, N.R.; Sharma, S.K.; McKay, C. Remote Raman spectroscopy for planetary exploration: A review. *Appl. Spectrosc.* **2012**, *66*, 137–150. [CrossRef] [PubMed]
15. Wang, A.; Freeman, J.J.; Jolliff, B.L.; Chou, I.-M. Sulfates on Mars: A systematic Raman spectroscopic study of hydration states of magnesium sulfates. *Geochim. Et Cosmochim. Acta* **2006**, *70*, 6118–6135. [CrossRef]
16. Haskin, L.A.; Wang, A.; Rockow, K.M.; Jolliff, B.L.; Korotev, R.L.; Viskupic, K.M. Raman spectroscopy for mineral identification and quantification for in situ planetary surface analysis: A point count method. *J. Geophys. Res. Planets* **1997**, *102*, 19293–19306. [CrossRef]

17. Nascimento-Dias, B. Aplicação da espectroscopia Raman na identificação de olivinas em meteoritos. *J. Exp. Tech. Instrum.* **2021**, *4*, 21–28. [CrossRef]

18. Maksimova, A.A.; Petrova, E.V.; Chukin, A.V.; Nogueira, B.A.; Fausto, R.; Szabó, Á.; Dankházi, Z.; Felner, I.; Gritsevich, M.; Kohout, T.; et al. Bjurböle L/LL4 ordinary chondrite properties studied by Raman spectroscopy, X-ray diffraction, magnetization measurements and Mössbauer spectroscopy. *Spectrochim. Acta Part A Mol. Biomol. Spectrosc.* **2021**, *248*, 119196. [CrossRef]

19. Xie, Z.; Sharp, T.G.; DeCarli, P.S. High-pressure phases in a shock-induced melt vein of the Tenham L6 chondrite: Constraints on shock pressure and duration. *Geochim. Et Cosmochim. Acta* **2006**, *70*, 504–515. [CrossRef]

20. Pittarello, L.; Baert, K.; Debaille, V.; Claeys, P. Screening and classification of ordinary chondrites by Raman spectroscopy. *Meteorit. Planet. Sci.* **2015**, *50*, 1718–1732. [CrossRef]

21. Alba-Aldave, L.; Cervantes-de la Cruz, K.; Sato-Berru, R.; Linares-López, C.; Reyes-Salas, M.; Ortega-Gutiérrez, F. Ca-poor Pyroxene Raman Characteristics in H Ordinary Chondrites. In Proceedings of the AIP Conference Proceedings 2–4 April 2009, Mainz, Germany, 2–4 April 2009; American Institute of Physics: College Park, MD, USA, 2009; Volume 1163, pp. 161–167. [CrossRef]

22. Kuebler, K.E.; Jolliff, B.L.; Wang, A.; Haskin, L.A. Extracting olivine (Fo–Fa) compositions from Raman spectral peak positions. *Geochim. Et Cosmochim. Acta* **2006**, *70*, 6201–6222. [CrossRef]

23. Huang, E.; Chen, C.; Huang, T.; Lin, E.; Xu, J.-A. Raman spectroscopic characteristics of Mg-Fe-Ca pyroxenes. *Am. Mineral.* **2000**, *85*, 473–479. [CrossRef]

24. Karki, B.; Duan, W.; Da Silva, C.; Wentzcovitch, R. Ab initio structure of $MgSiO^3$ ilmenite at high pressure. *Am. Mineral.* **2000**, *85*, 317–320. [CrossRef]

25. Lin, Y.; Kimura, M.; Miao, B.; Dai, D.; Monoi, A. Petrographic comparison of refractory inclusions from different chemical groups of chondrites. *Meteorit. Planet. Sci.* **2006**, *41*, 67–81. [CrossRef]

26. Xie, X.; Chen, M.; Wang, D. Shock-related mineralogical features and PT history of the Suizhou L6 chondrite. *Eur. J. Mineral.* **2001**, *13*, 1177–1190. [CrossRef]

27. Chen, M.; Sharp, T.G.; Goresy, A.E.; Wopenka, B.; Xie, X. The majorite-pyrope+ magnesiowüstite assemblage: Constraints on the history of shock veins in chondrites. *Science* **1996**, *271*, 1570–1573. [CrossRef]

28. Wesełucha-Birczyńska, A.; Żmudzka, M. Micro-Raman spectroscopy characterization of selected meteorites. *J. Mol. Struct.* **2008**, *887*, 253–261. [CrossRef]

29. Chakraborty, S. Diffusion Coefficients in Olivine, Wadsleyite and Ringwoodite. *Rev. Mineral. Geochem.* **2010**, *72*, 603–639. [CrossRef]

30. Rull, F.; Muñoz-Espadas, M.J.; Lunar, R.; Martínez-Frías, J. Raman spectroscopic study of four Spanish shocked ordinary chondrites: Cañellas, Olmedilla de Alarcón, Reliegos and Olivenza. *Philos. Trans. R. Soc. A: Math. Phys. Eng. Sci.* **2010**, *368*, 3153–3166. [CrossRef]

31. Hope, G.; Woods, R.; Munce, C. Raman microprobe mineral identification. *Miner. Eng.* **2001**, *14*, 1565–1577. [CrossRef]

32. Unsalan, O.; Altunayar-Unsalan, C. Shock–induced olivine–ringwoodite and plagioclase–maskelynite transformations in Bursa L6 chondrite: A Raman and ATR–FTIR spectroscopic study. *Spectrochim. Acta Part A: Mol. Biomol. Spectrosc.* **2020**, *240*, 118590. [CrossRef]

33. Foster, N.; Wozniakiewicz, P.J.; Price, M.C.; Kearsley, A.T.; Burchell, M.J. Identification by Raman spectroscopy of Mg–Fe content of olivine samples after impact at 6 km s− 1 onto aluminium foil and aerogel: In the laboratory and in Wild-2 cometary samples. *Geochim. Et Cosmochim. Acta* **2013**, *121*, 1–14. [CrossRef]

34. Harriss, K.H.; Burchell, M.J. A study of the observed shift in the peak position of olivine Raman spectra as a result of shock induced by hypervelocity impacts. *Meteorit. Planet. Sci.* **2016**, *51*, 1289–1300. [CrossRef]